Research Article | Vol. 32, No. 11 / 20 May 2024 / Optics Express 19076
Optics EXPRESS

High-harmonic spin-shearing interferometry for spatially resolved EUV magneto-optical spectroscopy

NATHAN J. BROOKS,[1,*] KEVIN M. DORNEY,[1] JENNIFER ELLIS,[1] ALEXANDER E. DENTON,[2] CHRISTIAN GENTRY,[1] SINÉAD A. RYAN,[1] QUYNH L. D. NGUYEN,[1] DREW W. MORRILL,[1] HENRY C. KAPTEYN,[1,3] AND MARGARET M. MURNANE[1]

[1]JILA, University of Colorado, 440 UCB, Boulder, Colorado 80309, USA
[2]COSINC-FAB, University of Colorado, 615 UCB, Boulder, Colorado 80309, USA
[3]KMLabs Inc., Boulder, Colorado 80309, USA
[*]nathan.brooks@colorado.edu

Abstract: We present a method for achieving hyperspectral magnetic imaging in the extreme ultraviolet (EUV) region based on high-harmonic generation (HHG). By interfering two mutually coherent orthogonally-polarized and laterally-sheared HHG sources, we create an EUV illumination beam with spatially-dependent ellipticity. By placing a magnetic sample in the beamline and sweeping the relative time delay between the two sources, we record a spatially resolved interferogram that is sensitive to the EUV magnetic circular dichroism of the sample. This image contains the spatially-resolved magneto-optical response of the sample at each harmonic order, and can be used to measure the magnetic properties of spatially inhomogeneous magnetic samples.

1. Introduction

The study of magnetic materials and their properties is important for a better fundamental understanding of magnetism as well as current and future technological applications. Understanding magnetic thin films, as but one example, is crucial for advancing magnetic storage devices, spintronics, and magnetic sensors. Circularly polarized light provides a powerful tool to probe the magnetic properties of thin films based on magneto-optical interactions. Specifically, spectroscopies based on the magneto-optical Kerr effect (MOKE) and magnetic circular dichroism (MCD) measure differential signals between orthogonal polarizations of light, making it possible to extract the average (i.e. non-site-specific) dynamic magnetic state using visible light [1], or to probe with element-selectivity at the characteristic absorption edges of magnetic materials using soft x-ray illumination [2]. Moreover, new spectro-microscopies and imaging techniques make it possible to dynamically probe and image magnetic materials [3]. In particular, ultrafast extreme UV (EUV) sources based on high harmonic generation (HHG) span many elemental absorption edges, which makes it possible to capture the fastest spin dynamics, spin transport, inter-site spin transfer and transport in alloys and multilayers, that can occur on few-femtosecond timescales on up [4–11]. To date, most EUV HHG studies have probed the spatially integrated dynamic response of materials, with spatial resolution ~100 μm. Alternatively, monochromatic imaging of magnetic samples has also been implemented [12,13]. However, many multi-element and/or spatially structured magnetic samples such as metalattices [14], skyrmions [15], spin ices [16], bit-patterned recording media [17], and exchange-coupled nanocomposites [18,19] can benefit from functional imaging at high spatial and temporal resolution.

In this work, we present a novel approach to measuring the EUV magneto-optical response of spatially inhomogeneous magnetic thin films, based on lateral shearing interferometry with

#521669 https://doi.org/10.1364/OE.521669
Journal © 2024 Received 15 Feb 2024; revised 28 Apr 2024; accepted 30 Apr 2024; published 9 May 2024

Optics EXPRESS

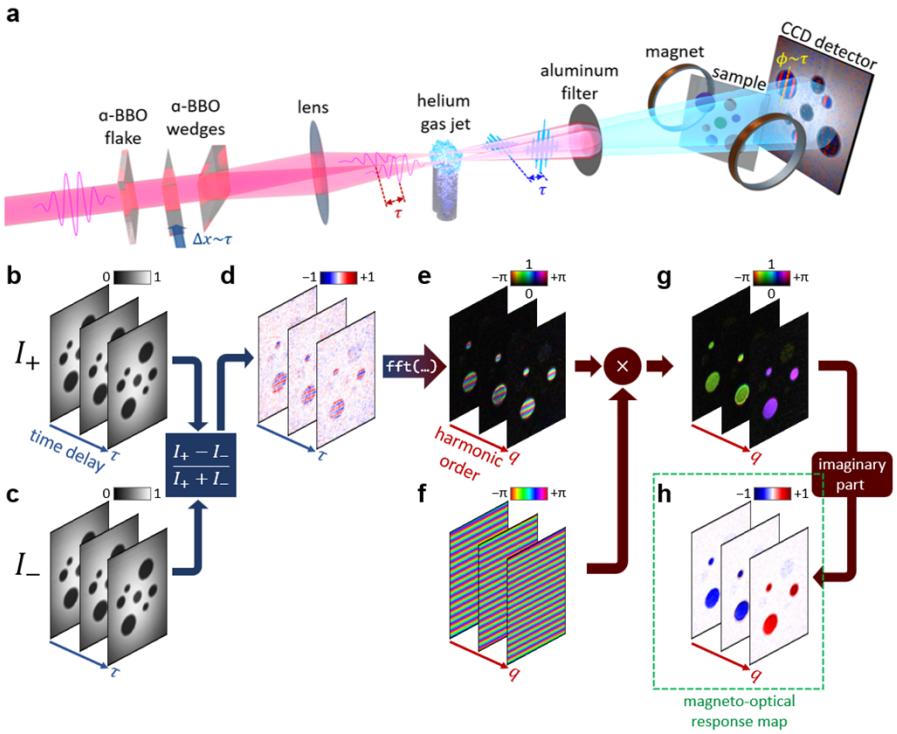

Fig. 1. | Principle of EUV spin shearing interferometry. a A common path interferometer based on birefringent optics produces laterally sheared laser pulses with orthogonal polarization and a relative time delay controlled by insertion of a wedge. These pulses drive HHG to produce orthogonally polarized EUV sources with the same shear, polarization, and time delay, which then diverge and overlap in the far field to produce an EUV field with spatially varying ellipticity. The transmission through a magnetic thin film sample in the presence of an external magnetic field is captured by a CCD detector. The time delay is scanned with a step size and extent determined by the desired spectral range and sampling. At each time delay, the magnetization direction is switched back and forth to acquire two image stacks, corresponding to **b** parallel, and **c** antiparallel magnetization directions with respect to the beam path. **d** The normalized difference of these image stacks gives fringes of magneto-optical contrast which shift across the sample as a function of time delay. **e** Fourier transforming with respect to time delay gives a complex image stack which is the spatially resolved MCD response modulated by a geometric shearing phase **f**. Removal of this phase **g** and taking the imaginary part **i** gives a stack of images showing the spatially resolved magneto-optical response of the sample at all harmonic wavelengths.

orthogonally polarized HHG sources (see Fig. 1). The interference of these sources creates a unique EUV structured polarization grating, with multiple contributing harmonic wavelengths, and spatially varying ellipticity including linear and circular polarizations [20]. This spatially varying ellipticity is converted to fringes of slight amplitude modulation upon transmission through a magnetized sample, due to the EUV magnetic circular dichroism effect (EUV-MCD). By precisely scanning the time delay between the orthogonally polarized HHG sources, we shift this amplitude modulation across the sample and thus obtain a pixel-resolved interferogram signal. This signal at a given pixel can be interpreted as the local EUV-MCD response of the sample, integrated over all harmonic orders. The individual harmonic wavelength contributions can then be digitally separated by a Fourier transform with respect to time delay, enabling spatially and

Optics EXPRESS

spectrally resolved magneto-optical analysis without the need for an EUV spectrometer. This work demonstrates the potential of polarization-structured HHG as a powerful approach for imaging magnetic thin films, opening up new opportunities for advancing our understanding of magnetic phenomena and for aiding the development of magnetic devices and technologies.

2. Concept

The coherence properties of HHG enable the transferring of the phase and polarization properties from an ultrafast driving laser to a multi-spectral EUV field, allowing the creation of a variety of tailored short-wavelength light sources [21–27]. One application of this unique property is the creation of phase-locked and laterally sheared harmonic sources [28], i.e. duplicated EUV light sources propagating in a parallel direction but separated transversely. This has enabled a variety of interesting applications, including molecular interferometry [29,30], wavefront characterization [31], and multi-wavelength coherent diffractive imaging [32]. These applications utilize the interference between parallel, linearly polarized HHG light sources. However, it is also possible to create laterally sheared HHG sources with **orthogonal** polarizations. In this case, the interference of the two sources gives rise to polarization interference including circularly polarized EUV light [20]. Here, we show that this unique polarization- (spin-)structured light source can be used in a scanning Fourier transform spectroscopy scheme [33] to create a multispectral, spatially resolved map of the magneto-optical response of magnetic thin films.

To start, we consider the EUV field produced by driving HHG with a pair of orthogonally polarized, laterally sheared, and relatively delayed (but otherwise identical and mutually coherent) driving lasers (Fig. 1(a)). Due to the coherence of the HHG process, the polarization and relative phase of the laser drivers are transferred to their respective HHG emission. Thus, in the source plane, the electric field can be written as a Fourier series over (odd) harmonic orders q,

$$\begin{aligned} E_{src}(x,y,t) &= E\left(x, y-\frac{s}{2}, t\right)\hat{x} + E\left(x, y+\frac{s}{2}, t-\tau\right)\hat{y} \\ &\propto \sum_{q=1,3,5\ldots}^{\infty}\left[E_q\left(x, y-\tfrac{s}{2}\right)\hat{x} + E_q\left(x, y+\tfrac{s}{2}\right)e^{-2\pi i\frac{qc\tau}{\lambda_0}}\hat{y}\right]e^{2\pi i\frac{qct}{\lambda_0}} \end{aligned} \tag{1}$$

where s is the shear distance (i.e, the separation between the two sources, here along the y-axis), x and y are the spatial coordinates, τ is the relative time delay, c is the speed of light, λ_0 is the driving laser wavelength. E_q is the spatial mode of the qth harmonic order, and generally includes all amplitude and phase factors which should be identical between the two sources, such as the intrinsic (dipole) harmonic phase. As the EUV emission propagates away from the source plane, the two sheared sources overlap and interfere. In the Fraunhofer regime, this is effectively a Fourier transform with respect to the spatial dimensions. Redefining the spatial coordinates x and y in the far field located a distance D from the source, we have

$$\begin{aligned} E_{far}(x,y,t) &\propto \sum_{q=1,3,5\ldots}^{\infty}\tilde{E}_q(x,y)\left(e^{2\pi i\frac{qsy}{2\lambda_0 D}}\hat{x} + e^{-2\pi i\left(\frac{qsy}{2\lambda_0 D}-\frac{qc\tau}{\lambda_0}\right)}\hat{y}\right) \\ &= \sum_{q=1,3,5\ldots}^{\infty}\tilde{E}_q(x,y)\left[\sin\left(2\pi\frac{q}{\lambda_0}\left(\frac{sy}{2D}-\frac{c\tau}{2}\right)\right)\hat{e}_{LCP} + \cos\left(2\pi\frac{q}{\lambda_0}\left(\frac{sy}{2D}-\frac{c\tau}{2}\right)\right)\hat{e}_{RCP}\right]e^{iq\omega_0 t} \end{aligned} \tag{2}$$

where in the second line we have rewritten in the basis of circular polarization, showing a sinusoidal oscillation between left circular polarization (LCP) and right circular polarization (RCP). As the period of interference is inversely proportional to the wavelength, the overall polarization structure of the spin grating is given by the superposition of all harmonic orders. Furthermore, the grating phase (i.e., the relative offset of the oscillation) is proportional to the relative time delay τ, and changing the time delay causes the entire polarization structure to shift in space.

Optics EXPRESS

Upon transmission through a magnetized thin film sample placed in the far field, the invisible polarization structure in the electric field is converted to amplitude modulation through the EUV-MCD effect. The modulation depth is dependent on contributions from both on- and off-resonance harmonics. We model this interaction with a wavelength- and circular polarization-dependent transmission function. For simplicity in this mathematical description, we neglect diffraction over the distance between the sample and the detector, which becomes less significant with increasing harmonic order. In this case, the signal recorded by the detector placed directly behind the sample is given by the time-averaged intensity,

$$I^{\pm}(x,y;\tau) \propto \sum_{q=1,3,5\ldots}^{\infty} |\tilde{E}_q(x,y)|^2 \left[1 \pm A_q(x,y)\sin\left(2\pi \tfrac{q}{\lambda_0}\left(\tfrac{sy}{D} - c\tau\right)\right)\right] \tag{3}$$

where I^+ and I^- are the detected intensities for parallel and antiparallel magnetization vector of the sample (Fig. 1(b)) relative to the direction of propagation, respectively. The first term in the brackets is the spectroscopic term, while the polarization-dependent EUV-MCD interaction is encapsulated in the second. To isolate the latter, we can calculate the normalized difference of two images with opposing magnetization directions,

$$\begin{aligned} A(x,y) &= \frac{I^+(x,y) - I^-(x,y)}{I^+(x,y) + I^-(x,y)} \\ &= \sum_{q=1,3,5\ldots}^{\infty} I_q(x,y)A_q(x,y)\sin\left(2\pi \tfrac{q}{\lambda_0}\left(\tfrac{sy}{D} - c\tau\right)\right) \end{aligned} \tag{4}$$

which gives the result for the normalized difference measurement at a fixed time delay. In this equation, I_q is the relative intensity fraction of the qth harmonic order, and A_q is the sample EUV-MCD asymmetry traditionally measured spectroscopically. Our goal here is to measure A_q as a function of space over all harmonic orders. To do so, we collect a series of these differential frames over a range of time delays τ (Fig. 1(c)) and Fourier transform along the corresponding axis. The result is a stack of complex-valued images (Fig. 1(d)) as a function of harmonic order q,

$$\tilde{A}_q(x,y) \propto iI_q(x,y)A_q(x,y)e^{2\pi i \frac{q}{\lambda_0}\left(\frac{sy}{D}\right)} \tag{5}$$

The rightmost phase factor is the result of the lateral shear between the two harmonic sources. Given a measurement of the shear distance s and source-detector distance D, it can be removed by multiplying by the conjugate phase (Fig. 1(e)). We note that recent work has shown that chromatic aberration in the HHG process may result in a wavelength-dependent shift ΔD on the order of a few cm [34]. For our experimental parameters and spectral region of interest, $D \gg \Delta D$, so this effect is expected to be small – therefore, we assume a fixed D for all wavelengths. However, it could become more important to account for this effect at shorter wavelengths or tighter focusing geometries. The resulting stack of images then consists of complex-valued EUV-MCD response maps of the sample (Fig. 1(f)) with phase equal to either $\pi/2$ or $-\pi/2$, corresponding to positive and negative EUV-MCD asymmetry, respectively. The presence of the imaginary unit i reflects the fact that the interferogram signal has a sine character and is thus asymmetric about time zero. Taking the imaginary part thus gives the magnetic asymmetry $A_q(x,y)$ (Fig. 1 g), weighted by the relative harmonic intensity $I_q(x,y)$ at each pixel. If the harmonic orders are of approximately equal weight in the spectral region of interest, or otherwise measured directly, quantitative EUV-MCD values can be obtained. However, even in the absence of such a calibration, this measurement can be used to make qualitative measurements sufficient for elemental identification (i.e. by determining at which energy the MCD signal changes sign) or quality inspection (i.e. identifying inhomogeneities due to sample growth problems such as uneven thickness, contamination, strain, different phases forming during annealing, etc. [35]).

Optics EXPRESS

3. Experiment

To experimentally demonstrate spatially resolved magneto-optical spectroscopy, we create a pair of orthogonally polarized HHG sources using a common path interferometer based on birefringent optics (Fig. 1(a)). The linearly polarized partial output of a high-power ultrafast regenerative amplifier (KMLabs Wyvern HE, central wavelength 790 nm, pulse duration 45 fs, maximum pulse energy 8 mJ, repetition rate 1 kHz) [31] is passed through a birefringent (a-BBO) plate with crystal axis oriented at 45° relative to the laser polarization, resulting in two orthogonally polarized pulses with equal power and a relative time delay. These pulses then pass through a pair of birefringent wedges (a-BBO), with crystal axes oriented at −45° so as to resynchronize the pulses in time. However, the second wedge is placed at a slight tilt angle (≈7°) to introduce an angular separation between the orthogonally polarized pulses. This wedge is placed in the back focal plane of a lens (f = 25 cm), creating spatially sheared and orthogonally polarized foci ($1/e^2$ diameter = 50 µm, separation s = 235 µm) in the front focal plane. These foci are set above a two-channel capillary (150 µm channel diameter) with separation matched to that of the foci, through which we flow helium gas (backing pressure 75 psi) to create a pair of identical gas targets. The emitted EUV light is separated from the driving laser by an aluminum filter (200 nm, Luxel) before illuminating the sample, placed a distance 1.47 m from the source, and an additional 5 cm to the detector for a total propagation distance of D = 1.52 m.

The sample is created by depositing magnetic thin films through a mask machined with circles of various diameters (200, 300, 500 µm) via thermal evaporation onto a 30 nm silicon nitride membrane (Fig. 2(a)). The 20 nm thick cobalt (Co) and nickel (Ni) islands are deposited in separate steps, with the mask rotated by 180° between depositions. A 15 nm thick, 300 µm diameter copper (Cu) island was patterned in the center. The nonmagnetic Cu has similar total transmission to the EUV light as the magnetic metals, and serves as a control to confirm that our technique is only sensitive to the magneto-optical properties of the sample. In order to observe the MCD contrast, the sample magnetization vector must have a parallel or antiparallel component relative to the direction of propagation. However, the magnetic thin film samples used in this experiment tend to only have in-plane magnetization. We thus place the sample at 45° relative to the incident beam to allow observation of the M-edge MCD effect. This geometry enables observation of the MCD contrast, albeit with a $\sqrt{2}$ reduction in the MCD signal. Additionally, the image observed on the camera is a 45° projection, resulting in a compression of the image along one dimension. We correct for this with a linear interpolation prior to the image reconstruction.

The transmitted are collected by an EUV-CCD (512 × 2048 pixels, 13.5 µm pixel size, Andor Newton) detector. A vacuum-coupled electromagnet is used to impose a switching magnetic field on the sample in order to make differential MCD measurements. For the current data, we averaged 70 frames in each magnetization direction over 200 equally spaced time delay points, covering a range of ± 2.65 fs centered at time zero. Each frame had an acquisition time of 3.6 seconds for a total acquisition time of approximately 28 hours. As the hyperspectral information is achieved through Fourier transform along the time delay axis, the spectral range and resolution are set by the time scan step size and extent, respectively. Based on the sampling parameters here, the hyperspectral image stack has a spectral spacing of 0.78 eV, and a spectral range of 78 eV. These parameters are chosen so as to adequately sample the spacing between the (odd) harmonic peaks of 3.11 eV, up to the aluminum edge at ∼72 eV. We note that using a more efficient geometry with optimized HHG flux [36] can significantly speed up the data acquisition process by orders of magnitude, which was not implemented for this demonstration experiment.

The spectrally integrated transmission of the raw EUV beam (Fig. 2(b), left) through different areas of the sample are observed to be similar – approximately 28% for Cu, 22% for Co, and 21% for Ni. Additionally, we experimentally observe faint interference fringes with a contrast of ∼2% even in the areas of the sample without magnetization (barely visible by eye in Fig. 2(b), left). This represents a departure from our theoretical model, in which the sheared sources should be

Optics EXPRESS

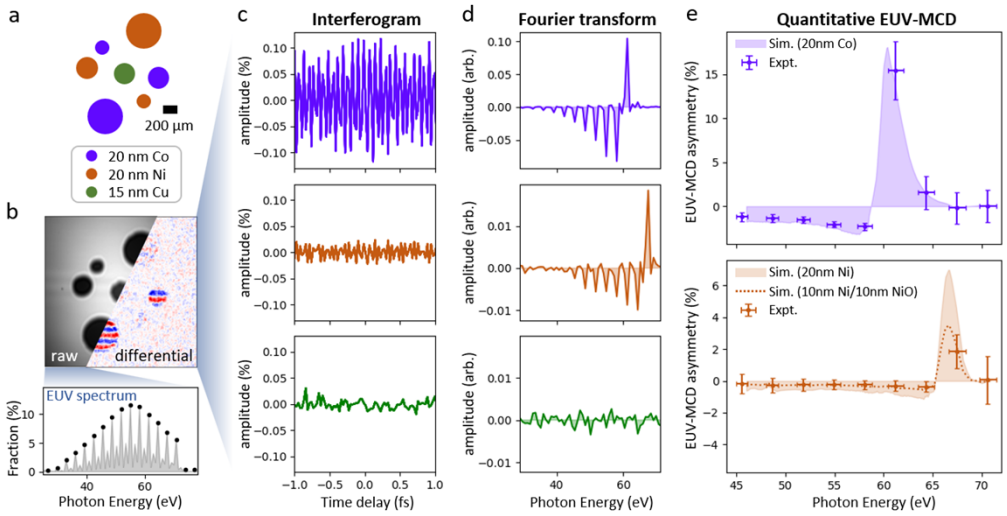

Fig. 2. Elemental identification based on magneto-optical contrast at the M-edge. a Design of the spatially inhomogeneous sample with both magnetic (Ni, Co) and nonmagnetic (Cu) regions. **b** Raw image (left) at a particular time delay, including residual intensity interference in the background (orange arrow) which can be used to measure the spectral content of the light source. A differential measurement between magnetizations reveals fringes of MCD contrast (right) within the magnetic elements. Sweeping the time delay causes these fringes to shift across the sample, creating **c** a spatially resolved interferogram signal, shown averaged over areas of each element. **d** The corresponding Fourier transforms give the EUV-MCD response, weighted by the relative wavelength fraction of each harmonic order. **e** Taking the values at the values at the harmonic peaks and using the spectral calibration from **b** gives quantitative EUV-MCD values (up to a single overall calibration factor) which are consistent with a multilayer calculation based on literature magneto-optical constants.

orthogonal and exhibit no intensity interference. Their observation here is the result of slight coupling between the sheared sources, resulting in slight polarization impurity. Similar to the expected EUV-MCD modulation, these "residual fringes" move across the beam as the time delay is scanned. The consequence of this is is that the differential measurement between opposing magnetizations is necessary in order to eliminate these "residual fringes" and observe the faint EUV-MCD signal in the magnetic parts of the sample (Fig. 2(b), right), which here have an order of magnitude smaller contrast ($< 0.2\%$ relative to the full beam intensity). However, it also brings a net benefit – the ability to measure the spectral content of the beam in different areas of the sample without additional measurements [33] (Fig. 2(b), inset).This is a useful calibration which enables quantitative assessment of the spatially resolved EUV-MCD.

Sweeping the time delay and calculating the normalized difference signal yields a magnetic interferogram signal at each pixel. To investigate the capability of our technique to distinguish between different magnetic and nonmagnetic elements, we first plot the interferogram signal (after compensation for the relative phase) averaged over areas of the sample known to be Co, Ni, and Cu (Fig. 2(c)). The magnetically active elements Co and Ni show clear sinusoidal oscillations as a function of time delay, while, the nonmagnetic Cu control area shows no such signal, confirming that the technique is sensitive only to the magneto-optical properties of the sample. Assuming the interferogram is centered correctly on time zero, the MCD signal is asymmetric within the sampling window, and thus a purely imaginary quantity under a Fourier transform (if the interferogram is not centered, the FT result contains a linear phase which is first estimated and

Optics EXPRESS

removed). Taking the imaginary portion of the FT result then gives a series of peaks describing the qualitative EUV-MCD response at the different harmonic orders (Fig. 2(d)). In the Co and Ni areas, these peaks exhibiting a gradual buildup and fast sign inversion characteristic of the magneto-optical asymmetry at the M-edge. We note that although the results at this point are only qualitative without a calibration for the spectrum, the signature of the buildup and sign inversion in the FT are still sufficient to distinguish between the Co and Ni portions of the sample.

In order to make our results more quantitative, we next carried out a calibration for the spectral intensity $I_q(x, y)$. To do this, we made use of the residual interference fringes described previously, using the method described in [33] to measure the relative strengths of the harmonic orders at different areas in the sample (inset in Fig. 2(b), corresponding to the bare portion of the sample). We use this measurement to rescale the relative harmonic peak values in the FT, along with a single overall normalization factor for the full data set (chosen here to match the ~61 eV harmonic H39 with the theoretical result). The resulting EUV-MCD values (Fig. 2(e)) can be compared to a simulation based on a multilayer calculation [37] (shaded curves) using literature values for the relevant magneto-optical constants [38]. The vertical error bars on the experimental data indicate the standard deviation within the population of each elements, and the horizontal error bars reflect an uncertainty in the harmonic energy corresponding to ±5 nm in the fundamental central wavelength. We observe that the MCD contrast observed for Ni (~2%) is weaker than Co (~15%), with a discrepancy significantly greater than what is expected based on the multilayer calculation. This likely indicates partial oxidation of the Ni portion of the sample due to elevated temperatures required in the thermal evaporation process. Indeed, we find that the observed contrast data is more consistent with the expected MCD from a 10 nm Ni/10 nm NiO multilayer (orange dashed curve), supporting this theory.

Next, we apply our reconstruction procedure to obtain a fully spatially resolved magneto-optical response map at all of the harmonic wavelengths. In addition to the steps described previously, we apply a high pass spatial filter to the individual frames to suppress the effects of large-scale beam fluctuations resulting from air currents or mechanical vibrations present in the real experiment (which could alternatively be eliminated using intensity normalization [10,11]). The images are then obtained by selecting the FFT frequency bin at each pixel corresponding the harmonic peak. Since for our sampling parameters the frequency bin width of 0.78 eV is close to the expected harmonic bandwidth in this spectral region, the images can be interpreted as the mean response over the harmonic order. As in the element-averaged data, the relative signals of the images should be divided by the spectral weights in order to be truly quantitative; however, doing so tends to amplify speckle noise and corrupt the signal in the weaker off-resonance harmonics. However, the unscaled results are still sufficient to measure different inhomogeneous spatial and spectral structure across a wide range of harmonic orders, H23-H43, spanning photon energies from 36-67 eV (Fig. 3). The sign inversions in the MCD contrast for the magnetically active Co and Ni portions of the sample near their respective M-edges are clearly visible, while the nonmagnetic copper and bare substrate areas of the sample do not show MCD contrast. This demonstrates the capability of our technique for measuring samples with spatially varying magneto-optical response, such as the multi-element magnetic structures as shown here, as well as samples with suspected inhomogeneities due to laser irradiation or oxidation. We note that the latter is a particularly interesting case, as such inhomogeneities may be difficult to detect with purely spectroscopic techniques.

We next investigated the spatial resolution of our technique, and the spatial scales on which it can be used to observe spatial inhomogeneities in the magnetic signal. In the current "projection" geometry, the physical limit on spatial resolution is given by twice the (13.5 μm) pixel size of our detector, equal to 27 μm. Practically, we expect a further decrease in resolution due to low signal-to-noise ratio and diffraction over the 5 cm distance between the sample and detector. With this in mind, we analyzed our images using Fourier ring correlation (FRC) [39]. Briefly, the FRC

Optics EXPRESS

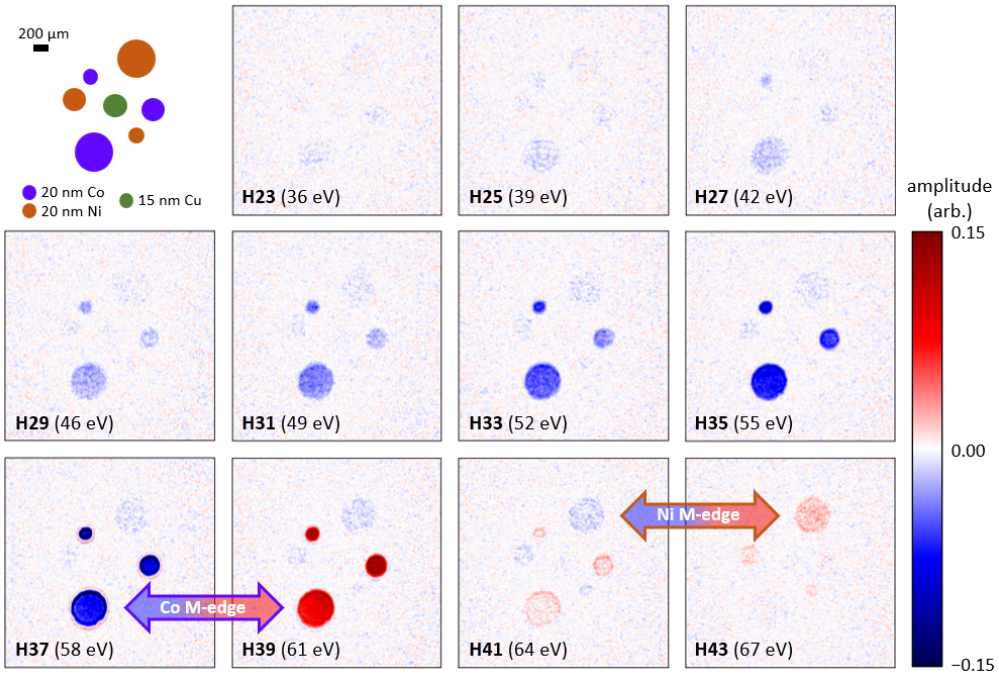

Fig. 3. Multispectral EUV-MCD image stack. The reconstruction process produces an EUV MCD image stack at all of the harmonic wavelengths present in the light source. There is a clear gradual buildup and sign inversion in the MCD contrast for the magnetically active cobalt and nickel portions of the sample near their respective M-edges, while the nonmagnetic copper and clear areas of the sample exhibit no signal.

estimates the effective spatial resolution of an imaging technique by looking at the repeatability of the spatial power spectrum as a function of spatial frequency. To carry out the FRC for our technique, we divided the data into two halves, and reconstructed independent sets of magnetic images. For the images corresponding to the three harmonic energies nearest the Co M-edge (H35, H37, H39, Fig. 4(a)), we calculated the spatial power spectrum by a Fourier transform in the spatial dimensions. This is shown in Fig. 4(b) as a log scale RGB image, where the the power spectra of H35, H37, and H39 are shown in blue, green, and red channels, respectively. The spatial power spectrum falls off at higher spatial frequencies, with H37 (green) extending somewhat further out than the others. This is borne out by the FRC analysis (Fig. 4(c)), which shows a higher effective resolution for H37 (45 µm) than H35 (79 µm) and H39 (71 µm).

With this in mind, we examine the spatial structure within the 500 µm Co disk (Fig. 4(d)). All three harmonics indicate that the magnitude of the MCD effect decreases towards the bottom of the disk for a total drop in signal of about 30%, as indicated by the lineout in Fig. 4(e) (where H39 is inverted in order for more intuititve comparison with the others). The consistency of this observation across the different wavelengths is a strong indication of inhomogeneity in this part of the sample, possibly due to uneven deposition or oxidation level. Also visible in Fig. 4(d) and 4(e) is a very interesting behavior in the periphery of the Co disks at the pre-edge harmonic H37. Specifically, the H37 image shows strongly modulated and even inverted contrast near the edges of the Co disk (orange arrow). This area of the image is strongly affected by near-field diffraction effects due to the presence of the hard edge (visible as well in the raw data), and so should not be interpreted as a portion of the sample having an inverted magneto-optical response. The inverted contrast arises as a result of the primary diffraction order, which is visible as a bright ring around

Optics EXPRESS

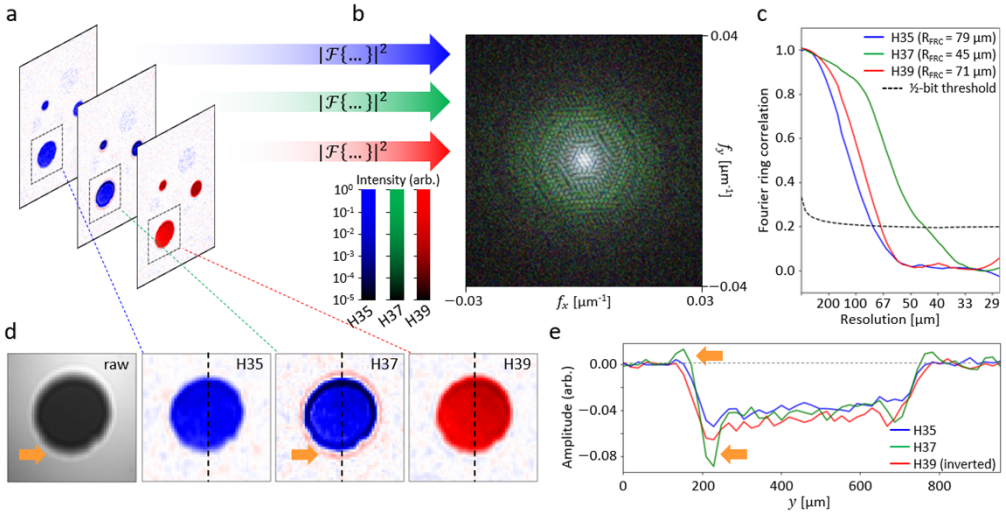

Fig. 4. Spatial resolution analysis of multispectral EUV-MCD imaging. **a** Magnetic images corresponding to the three harmonics nearest the Co M-edge (H35, H37, H39) are Fourier transformed in x and y to give the spatial power spectrum **b** at each harmonic order, with their intensities shown in log scale as the blue, green, and red channels of the color image, respectively. This procedure is repeated for two independent subsets of data and used to calculate the Fourier ring correlation (FRC) at each harmonic order **c**, providing an estimate on the effective spatial resolution of the technique via the FRC cutoff resolution R_{FRC}, given by intersection with the 1/2-bit threshold curve. **d** A closeup of the 500 μm Co disk, with raw data shown for comparison, and **e** associated line profile around the dashed line, show inhomogeneous behavior including a ramp in MCD signal over the disk between the three harmonic orders, as well as enhanced near-field diffraction from the edges at H37 (orange arrows in **d** and **e**).

the disk in the raw image (Fig. 4(d), left). The strength of diffraction is expected to vary inversely with the transmission of the disk, hence the inverted contrast. What it does indicate, however, is that diffraction from the edges is strongly enhanced at H37, significantly larger even than H39 which has the largest overall EUV-MCD contrast. Given that the average SNR is approximately equal for the three harmonic orders analyzed here, this clear difference in behavior appears to a resonant enhancement in scattering from the edge of the disks. Although exploring the physical mechanism for this is beyond the scope of this work, we note this observation is made possible due to the unique combination of spatial and spectral resolution provided by our technique.

4. Discussion

In this work, we have introduced a novel technique based on spin shearing interferometry with a polarization structured HHG light source, which enables the measurement of spatially resolved magneto-optical contrast in the EUV. In contrast to previous magneto-optical techniques for this wavelength range, this technique is able to measure with both spatial and spectral resolution, enabling the characterization of inhomogeneous magnetic thin films. Beyond this initial demonstration, we envision numerous ways in which this technique could be improved. The main limitations of the technique shown here are the low spatial resolution, and the long time required for data acquisition across a long series of time delay. The spatial resolution of the technique is here is limited by the CCD pixel size of 13.5 μm, as well as diffraction over the distance (5 cm) between the sample and detector. We note that future work will involve

Optics EXPRESS

enhancing the resolution by moving beyond the simple projection geometry and integrating coherent diffractive imaging for diffraction-limited resolution [40,41]. The data acquisition speed can likely be improved by the application of compressive sensing [42,43]. This would basically involve replacing the sampling at fixed intervals of time delay with a random sampling scheme, and the use of an optimization routine in order to reconstruct the EUV-MCD spectrum at each pixel. Finally, the EUV flux can be significantly enhanced by using a more efficient geometry [36] with good differential pumping to avoid reabsorption of the harmonics by the gas.

In addition, although the use of a differential measurement is useful to isolate the magnetic signal from the larger nonmagnetic background, in principle it should be possible to obtain the same information without it, i.e., with only a single measurement at each time delay. This would remove the need to magnetically saturate the sample, thus opening the door to studying magnetic domains. In practice, the differential measurement is found to be necessary due to slight coupling between the sheared HHG sources. This could be mitigated by proper wavefront shaping of the HHG sources to ensure they are completely independent. Alternatively, the differential measurement could be carried out instead by physical 180° rotation of the sample. This would allow the differential signal to be required without the need to magnetically saturate the sample; however, it would require precise registration similar to that required for tomographic imaging.

Finally, we note that for many thin film samples deposited on optically thick substrates, transmission mode measurements are not feasible. For such samples, this measurement technique could also be adapted to reflection mode, in which the magneto-optical Kerr effect (MOKE) would provide the contrast mechanism. By tuning the harmonic orders [11], the number and location of sampled data points can be optimized to give further information about the sample absorption across the M-edge. Finally, soft x-ray supercontinua could also be used to fill in the gaps between harmonic orders [44,45], enabling EUV/SXR "white light" magnetic spectroscopy extending to the L-edges of the transition metals, as well as the M-edges of the rare-earth magnetics [46,47].

Funding. A U.S. Department of Energy Basic Energy Sciences X-Ray Scattering Program Award (DE-SC0002002) grant supported the magnetic sample and simulations performed for this research. The hyper spectral imaging research was supported by an Air Force Office of Scientific Research grant under Award No (FA9550-23-1-0281). The imaging setup was supported by STROBE: a National Science Foundation and Technology Center Award (DMR-1548924).

Disclosures. Alternate email address for NJB: nbrooks3@gmail.com. Current address for NJB: Institute of Atomic and Molecular Sciences (IAMS), Academia Sinica, Taipei 10617, Taiwan; Current address for JE: HRL Laboratories, Malibu, California 90265, USA; Current address for KMD: Imec, Kapeldreef 75, 3001 Leuven, Belgium; Current address for QLDN: Stanford PULSE Institute and Linac Coherent Light Source, SLAC National Accelerator Laboratory and Stanford University, Menlo Park, California 94025, USA; Current address for AD: Stanford Nanofabrication Facility, Stanford, CA 94305, USA

Data availability. Data underlying the results presented in this paper are not publicly available at this time but may be obtained from the authors upon reasonable request.

References

1. E. Beaurepaire, J.-C. Merle, A. Daunois, *et al.*, "Ultrafast Spin Dynamics in Ferromagnetic Nickel," Phys. Rev. Lett. **76**(22), 4250–4253 (1996).
2. G. Schutz, W. Wagner, W. Wilhelm, *et al.*, "Absorption of Circularly Polarized X Rays in Iron," Phys. Rev. Lett. **58**(7), 737–740 (1987).
3. J. Stöhr and H. C. Siegmann, *Magnetism: From Fundamentals to Nanoscale Dynamics*, 1st ed. (Springer Berlin, Heidelberg, 2006).
4. P. Tengdin, C. Gentry, A. Blonsky, *et al.*, "Direct light-induced spin transfer between different elements in a spintronic Heusler material via femtosecond laser excitation," Sci. Adv. **6**(3), eaaz1100 (2020).
5. W. You, P. Tengdin, C. Chen, *et al.*, "Revealing the Nature of the Ultrafast Magnetic Phase Transition in Ni by Correlating Extreme Ultraviolet Magneto-Optic and Photoemission Spectroscopies," Phys. Rev. Lett. **121**(7), 077204 (2018).
6. P. Tengdin, W. You, C. Chen, *et al.*, "Critical behavior within 20 fs drives the out-of-equilibrium laser-induced magnetic phase transition in nickel," Sci. Adv. **4**(3), 1–9 (2018).
7. E. Turgut, C. La-O-Vorakiat, J. M. Shaw, *et al.*, "Controlling the competition between optically induced ultrafast spin-flip scattering and spin transport in magnetic multilayers," Phys. Rev. Lett. **110**(19), 197201 (2013).

Optics EXPRESS

8. C. La-O-Vorakiat, M. Siemens, M. M. Murnane, *et al.*, "Ultrafast demagnetization dynamics at the M edges of magnetic elements observed using a tabletop high-harmonic soft X-ray source," Phys. Rev. Lett. **103**(25), 257402 (2009).
9. C. La-O-Vorakiat, E. Turgut, C. A. Teale, *et al.*, "Ultrafast demagnetization measurements using extreme ultraviolet light: Comparison of electronic and magnetic contributions," Phys. Rev. X **2**(1), 011005 (2012).
10. P. C. Johnsen, S. A. Ryan, C. Gentry, *et al.*, "A beamline for ultrafast extreme ultraviolet magneto-optical spectroscopy in reflection near the shot noise limit," Rev. Sci. Instrum. **94**(3), 1 (2023).
11. S. A. Ryan, P. C. Johnsen, M. F. Elhanoty, *et al.*, "Optically controlling the competition between spin flips and intersite spin transfer in a Heusler half-metal on sub-100-fs time scales," Sci. Adv. **9**(45), eadi1428 (2023).
12. O. Kfir, S. Zayko, C. Nolte, *et al.*, "Nanoscale magnetic imaging using circularly polarized high-harmonic radiation," Sci. Adv. **3**(12), eaao464 (2017).
13. S. Zayko, O. Kfir, M. Heigl, *et al.*, "Ultrafast high-harmonic nanoscopy of magnetization dynamics," Nat. Commun. **12**(1), 6337 (2021).
14. A. Rana, C. T. Liao, E. Iacocca, *et al.*, "Three-dimensional topological magnetic monopoles and their interactions in a ferromagnetic meta-lattice," Nat. Nanotechnol. **18**(3), 227–232 (2023).
15. S. Woo, K. Litzius, B. Krüger, *et al.*, "Observation of room-temperature magnetic skyrmions and their current-driven dynamics in ultrathin metallic ferromagnets," Nat. Mater. **15**(5), 501–506 (2016).
16. J. S. Woods, X. M. Chen, R. V. Chopdekar, *et al.*, "Switchable X-Ray Orbital Angular Momentum from an Artificial Spin Ice," Phys. Rev. Lett. **126**(11), 117201 (2021).
17. T. R. Albrecht, H. Arora, V. Ayanoor-Vitikkate, *et al.*, "Bit-patterned magnetic recording: Theory, media fabrication, and recording performance," IEEE Trans. Magn. **51**(5), 1 (2015).
18. G. Barrera, P. Tiberto, P. Allia, *et al.*, "Magnetic properties of nanocomposites," Appl. Sci. **9**(2), 212 (2019).
19. F. Liu, Y. Hou, and S. Gao, "Exchange-coupled nanocomposites: Chemical synthesis, characterization and applications," Chem. Soc. Rev. **43**(23), 8098–8113 (2014).
20. J. L. Ellis, K. M. Dorney, D. D. Hickstein, *et al.*, "High harmonics with spatially varying ellipticity," Optica **5**(4), 479 (2018).
21. C. Hernandez-Garcia, A. Picon, J. San Roman, *et al.*, "Attosecond extreme ultraviolet vortices from high-order harmonic generation," Phys. Rev. Lett. **111**(8), 083602 (2013).
22. L. Rego, K. M. Dorney, N. J. Brooks, *et al.*, "Generation of extreme-ultraviolet beams with time-varying orbital angular momentum," Science **364**(6447), 1–26 (2019).
23. F. Kong, C. Zhang, H. Larocque, *et al.*, "Vectorizing the spatial structure of high-harmonic radiation from gas," Nat. Commun. **10**(1), 2020 (2019).
24. L. Rego, N. J. Brooks, Q. L. D. Nguyen, *et al.*, "Necklace-structured high-harmonic generation for low-divergence, soft x-ray harmonic combs with tunable line spacing," Sci. Adv. **8**(5), eabj7380 (2022).
25. R. A. Bartels, A. Paul, H. Green, *et al.*, "Generation of Spatially Coherent Light at Extreme Ultraviolet Wavelengths," Science **297**(5580), 376–378 (2002).
26. O. Kfir, P. Grychtol, E. Turgut, *et al.*, "Generation of bright phase-matched circularly-polarized extreme ultraviolet high harmonics," Nat. Photonics **9**(2), 99–105 (2015).
27. T. Fan, P. Grychtol, R. Knut, *et al.*, "Bright circularly polarized soft X-ray high harmonics for X-ray magnetic circular dichroism," Proc. Natl. Acad. Sci. U.S.A. **112**(46), 14206–14211 (2015).
28. R. Zerne, C. Altucci, M. Bellini, *et al.*, "Phase-Locked High-Order Harmonic Sources," Phys. Rev. Lett. **79**(6), 1006–1009 (1997).
29. X. Zhou, R. Lock, W. Li, *et al.*, "Molecular recollision interferometry in high harmonic generation," Phys. Rev. Lett. **100**(7), 073902 (2008).
30. X. Zhou, R. Lock, N. Wagner, *et al.*, "Elliptically polarized high-order harmonic emission from molecules in linearly polarized laser fields," Phys. Rev. Lett. **102**(7), 073902 (2009).
31. D. R. Austin, T. Witting, C. A. Arrell, *et al.*, "Lateral shearing interferometry of high-harmonic wavefronts," Opt. Lett. **36**(10), 1746 (2011).
32. G. S. M. Jansen, A. de Beurs, X. Liu, *et al.*, "Diffractive shear interferometry for extreme ultraviolet high-resolution lensless imaging," Opt. Express **26**(10), 12479 (2018).
33. G. S. M. Jansen, D. Rudolf, L. Freisem, *et al.*, "Spatially resolved Fourier transform spectroscopy in the extreme ultraviolet," Optica **3**(10), 1122 (2016).
34. X. Liu, A. Pelekanidis, M. Du, *et al.*, "Observation of chromatic effects in high-order harmonic generation," Phys. Rev. Res. **5**(4), 043100 (2023).
35. F. C. S. da Silva, C. M. Wang, and D. P. Pappas, "Interlaboratory Comparison of Magnetic Thin Film Measurements," J. Res. Natl. Inst. Stand. Technol. **108**(2), 125–134 (2003).
36. A. Rundquist, C. G. Durfee, Z. Chang, *et al.*, "Phase-Matched Generation of Coherent Soft X-rays," Science **280**(5368), 1412–1415 (1998).
37. J. Zak, E. R. Moog, C. Liu, *et al.*, "Magneto-optics of multilayers with arbitrary magnetization directions," Phys. Rev. B **43**(8), 6423–6429 (1991).
38. F. Willems, S. Sharma, C. V. Korff Schmising, *et al.*, "Magneto-Optical Functions at the 3p Resonances of Fe, Co, and Ni: Ab initio Description and Experiment," Phys. Rev. Lett. **122**(21), 217202 (2019).
39. M. Van Heel and M. Schatz, "Fourier shell correlation threshold criteria," J. Struct. Biol. **151**(3), 250–262 (2005).

Optics EXPRESS

40. S. Witte, V. T. Tenner, D. W. Noom, *et al.*, "Lensless diffractive imaging with ultra-broadband table-top sources: From infrared to extreme-ultraviolet wavelengths," Light: Sci. Appl. **3**(3), e163 (2014).
41. G. J. Williams, H. M. Quiney, B. B. Dhal, *et al.*, "Fresnel coherent diffractive imaging," Phys. Rev. Lett. **97**(2), 025506 (2006).
42. E. van den Berg and M. P. Friedlander, "Sparse Optimization with Least-Squares Constraints," SIAM J. Optim. **21**(4), 1201–1229 (2011).
43. O. Katz, J. M. Levitt, and Y. Silberberg, "Compressive Fourier Transform Spectroscopy," in *Frontiers in Optics 2010/Laser Science XXVI*, (Optica Publishing Group, 2010), p. paper FTuE3.
44. M. C. Chen, P. Arpin, T. Popmintchev, *et al.*, "Bright, coherent, ultrafast soft x-ray harmonics spanning the water window from a tabletop light source," Phys. Rev. Lett. **105**(17), 173901 (2010).
45. T. Popmintchev, M.-C. Chen, D. Popmintchev, *et al.*, "Bright Coherent Ultrahigh Harmonics in the keV X-ray Regime from Mid-Infrared Femtosecond Lasers," Science **336**(6086), 1287–1291 (2012).
46. M. Borchert, D. Engel, C. von Korff Schmising, *et al.*, "X-ray magnetic circular dichroism spectroscopy at the Fe L edges with a picosecond laser-driven plasma source," Optica **10**(4), 450 (2023).
47. G. Fan, K. Légaré, V. Cardin, *et al.*, "Ultrafast magnetic scattering on ferrimagnets enabled by a bright Yb-based soft x-ray source," Optica **9**(4), 399 (2022).